REPORT DOCUMENTATION PAGE

Form Approved
OMB No. 0704-0188

1. REPORT DATE *(DD-MM-YYYY)*	2. REPORT TYPE	3. DATES COVERED *(From - To)*
05-02-2007	REPRINT	

4. TITLE AND SUBTITLE
Passive Optical Diagnostic of Xe-propelled Hall Thrusters. II. Collisonal-Radiative Model

5a. CONTRACT NUMBER

5b. GRANT NUMBER

5c. PROGRAM ELEMENT NUMBER
61102F

6. AUTHOR(S)
G. F. Kaabadzhak*, Y. Chiu and R.A. Dressler

5d. PROJECT NUMBER
2303

5e. TASK NUMBER
RS

5f. WORK UNIT NUMBER
A1

7. PERFORMING ORGANIZATION NAME(S) AND ADDRESS(ES)
Air Force Research Laboratory/VSBXT
29 Randolph Road
Hanscom AFB MA 01731-3010

8. PERFORMING ORGANIZATION REPORT NUMBER
AFRL-VS-HA-TR-2007-1008

9. SPONSORING / MONITORING AGENCY NAME(S) AND ADDRESS(ES)

10. SPONSOR/MONITOR'S ACRONYM(S)

11. SPONSOR/MONITOR'S REPORT NUMBER(S)

12. DISTRIBUTION / AVAILABILITY STATEMENT
Approved for Public Release; Distribution Unlimited

*TSNIIMASH, Pionerskaya, Korolev, Moscow Region, Russia

13. SUPPLEMENTARY NOTES
REPRINTED FROM: Journal of Applied Physics, Vol 99, 113305 (2006).

14. ABSTRACT

A collisional radiative model is presented for analyzing the xenon-propelled Hall thruster optical radiation based on apparent electron and ion-impact emission cross sections associated with lines in the visible and near-infrared region of the spectrum. The emission cross sections of selected near-infrared emission lines are incorporated in a collisional-radiative model. The effect of stepwise excitation via metastable states on the derived line intensities for emissions from XeI $5p^5 6p(6p')$ levels is evaluated. Meanwhile, visible XeII emissions are shown to provide plasma densities at high electron temperature conditions. The electron temperature and spatial ion number density distribution were determined from the luminescence spectra measured in the discharge and plume near-field plasma of the Hall thruster, the TSNIIMASH D-55 anode layer thruster. The results are in good agreement with the probe measurement data and simulations reported in the literature for the same thruster. The analysis of the Hall thruster XeI near-infrared spectra demonstrates that the neglect of ion-atom collisions results in an erroneous electron temperature determination at electron temperatures below 10 eV. © *2006 American Institute of Physics*. [DOI: 10.1063/1.2195019]

15. SUBJECT TERMS
Hall thrusters, Xenon plasma, Electron emission excitation cross sections, Ion collision-induced emission excitation cross sections, Xe, electric propulsion, radiation trapping

16. SECURITY CLASSIFICATION OF:			17. LIMITATION OF ABSTRACT	18. NUMBER OF PAGES	19a. NAME OF RESPONSIBLE PERSON
a. REPORT	b. ABSTRACT	c. THIS PAGE			R. Dressler
UNCLAS	UNCLAS	UNCLAS	SAR		19b. TELEPHONE NUMBER *(include area code)* 781-377-2332

JOURNAL OF APPLIED PHYSICS 99, 113305 (2006)

Passive optical diagnostic of Xe propelled Hall thrusters. II. Collisional-radiative model

George F. Karabadzhak
TSNIIMASH, Pionerskaya 4, Korolev, Moscow 141070, Russia

Yu-hui Chiu and Rainer A. Dressler[a)]
Air Force Research Laboratory, Space Vehicles Directorate, Hanscom AFB, Massachusetts 01731

(Received 23 August 2005; accepted 13 March 2006; published online 9 June 2006)

A collisional radiative model is presented for analyzing the xenon-propelled Hall thruster optical radiation based on apparent electron and ion-impact emission cross sections associated with lines in the visible and near-infrared region of the spectrum. The emission cross sections of selected near-infrared emission lines are incorporated in a collisional-radiative model. The effect of stepwise excitation via metastable states on the derived line intensities for emissions from XeI $5p^5 6p(6p')$ levels is evaluated. Meanwhile, visible XeII emissions are shown to provide plasma densities at high electron temperature conditions. The electron temperature and spatial ion number density distribution were determined from the luminescence spectra measured in the discharge and plume near-field plasma of the Hall thruster, the TSNIIMASH D-55 anode layer thruster. The results are in good agreement with the probe measurement data and simulations reported in the literature for the same thruster. The analysis of the Hall thruster XeI near-infrared spectra demonstrates that the neglect of ion-atom collisions results in an erroneous electron temperature determination at electron temperatures below 10 eV. © *2006 American Institute of Physics*. [DOI: 10.1063/1.2195019]

I. INTRODUCTION

The extraction of plasma microparameters from spectral line intensities observed in the radiation emanating from xenon propelled Hall effect thruster (HET) plasmas requires a collisional radiative model (CRM) that takes all relevant excitation and deexcitation mechanisms into account. While in many cases the assumption of equilibrated electron energy distributions is justifiable, this cannot be stated for the atom and ion electronic state distributions, as previously reported.[1–3] For strong emission lines in the rarefied conditions of the HET plasma, the corona radiation model[4] may be considered as a starting point for an approximate CRM. The model assumes population of a particular state through electronic collisions and cascade radiative transitions from upper excited states, while depopulation of all excited states goes through radiative decay. In many earlier HET optical diagnostic studies a corona model was applied or assumed. Only few efforts are known to us that implemented a more complex radiation model to analyze a HET xenon plasma.[5,6] Among the corona model studies, Meezan *et al.*[7] are the sole authors that discussed the appropriateness of the model at the particular conditions.

Due to the complexity of the processes involved in HET xenon plasmas, the corona approximation usually falls short in rendering many of the plasma emission lines. One source of the problem is the very small energy intervals of XeI excited levels such as the $np^5(n+1)p$ and np^5nd states. Consequently, low-energy electrons can have very high probabilities in inducing transitions between these states. Another source of problems in the corona model is the possibility of stepwise excitation via metastable states, the importance of which has been previously demonstrated for xenon.[8] Bugrova *et al.*[3] also found that the corona model failed to describe the intensity of some plasma emissions in the ionization region of a stationary plasma thruster (SPT). They introduced a more complex CRM including stepwise excitation, and obtained a better agreement with experiment. Meanwhile, a final important shortcoming of the corona model is the neglect of heavy particle collisions, which have recently been proposed to play an important role in the emission excitation process in HET plasmas given the significant cross sections at the respective high ion energies.[9]

A major deficiency of all models has been a lack of experimentally determined emission excitation cross sections for all relevant Xe plasma processes. In a companion paper (Part I),[10] we report apparent emission cross sections associated with electron- and ion-Xe atom collisions for a set of near-infrared (NIR) and visible (VIS) lines. Since the reported cross sections include cascades from states above the upper radiating state, they incorporate the information of a significant fraction of the level-to-level radiation kinetics and the related level populations. In the present paper, we demonstrate how the use of these cross sections considerably simplifies a CRM involving the XeI NIR lines. The proposed CRM includes a stepwise excitation mechanism without an explicit knowledge of the cross sections for metastable excitation and excitation out of metastable states. The proposed model also clearly confirms earlier assertions[9] that the inclusion of ion processes is relevant for properly determining an electron temperature in plasma regions with relatively low characteristic electron temperatures.

After discussing the salient features of the model, it is applied to determining the electron temperature and charge

[a)]Electronic mail: dressler@hanscom.af.mil

density distribution in a TSNIIMASH D-55 anode layer (TAL) thruster.[11–14] We conclude the paper with a discussion on the benefits and limitations of the present diagnostic method, and provide suggestions for further improvements of the model.

II. COLLISIONAL RADIATIVE MODEL

A. General model

In this section, a CRM is developed to permit quantitative analysis of a HET plasma based on passive optical measurements. A CRM establishes the relationship between the HET microparameters, such as particle number densities and electron energies, and the optical radiation observed in the HET plasma. As delineated in Part I, the optical radiation is caused primarily by the following collision processes:

$$e^- + \mathrm{Xe}(p) \rightarrow \mathrm{Xe}^* + e^-, \tag{1}$$

$$\rightarrow \mathrm{Xe}^{q+*} + (q+1)e^-, \tag{2}$$

$$e^- + \mathrm{Xe}^+(p) \rightarrow \mathrm{Xe}^{q+*} + qe^-, \tag{3}$$

$$\mathrm{Xe}^+ + \mathrm{Xe} \rightarrow \mathrm{Xe}^{+*} + \mathrm{Xe}^*, \tag{4}$$

$$\mathrm{Xe}^{2+} + \mathrm{Xe} \rightarrow \mathrm{Xe}^{2+*} + \mathrm{Xe}^*, \tag{5}$$

$$\rightarrow \mathrm{Xe}^{+*} + \mathrm{Xe}^{+*}, \tag{6}$$

where the asterisks in processes (1)–(6) signify excited species that either lead to optical emissions or long-lived metastables that transfer the excitation in subsequent electronic or atomic collisions, q identifies the charge state, and p identifies all long-lived states, i.e., ground and metastable states.

The plasma radiation intensity per unit volume for a specific emission line at wavelength, λ, may be approximated by

$$J_\lambda = \frac{hc}{4\pi\lambda} N_0 N_e \left[\sum_p \frac{N_p}{N_0} \int_0^\infty f_e(E_e)\sigma_{ep}^\lambda(E_e)u_e dE_e + \sum_q \frac{N_q}{N_e} \int_0^\infty f_q(E_q)\sigma_q^\lambda(E_q)u_q dE_q \right]. \tag{7}$$

N_e, N_q, N_p, and N_0 are number densities of the electrons, ions, and xenon atoms in state p and all xenon atoms, respectively. $f_e(E_e)$ and $f_q(E_q)$ are the electron and ion energy distribution functions, respectively, normalized to unity. $\sigma_{ep}^\lambda(E_e)$ is the cross section for an electron with energy, E_e, to excite a Xe atom or ion from the lower state p to produce radiation at λ. $\sigma_q^\lambda(E_q)$ is the cross section for an ion with charge q and energy, E_q, to excite an atom to produce radiation at λ. u_e and u_q are the electron and ion velocities, respectively.

Equation (7) assumes that the states, i, excited by electron and ion collisions, are depopulated through radiation decay only. Clearly, this assumption is not justified for some xenon atomic and ionic states. The radiation decay condition may be expressed algebraically as

$$\tau_{\mathrm{rad},i}\nu_{\mathrm{dex},i} \ll 1 \text{ or } A_i = \sum_k A_{ik} \gg \nu_{\mathrm{dex},i}, \quad k < i, \tag{8}$$

where $\tau_{\mathrm{rad},i}$ is the radiative lifetime of the upper ith level, $\nu_{\mathrm{dex},i}$ is the collisional quenching frequency of the excited ith level, and A_{ik} is the Einstein coefficient for the $i \rightarrow k$ spontaneous emission transition. Although all plasma particles can quench a state, electron collision frequencies are significantly higher than heavy particle collision frequencies at HET plasma conditions. Consequently, condition (8) may be rewritten as

$$A_i \gg N_e \int_0^\infty f_e(E_e)\sigma_{de}(E_e)u_e dE_e = N_e k_{de}, \tag{9}$$

where $\sigma_{de}(E_e)$ is the electron collision depopulation cross section for the ith level, and k_{de} is the associated rate coefficient. The electron collision depopulation rate coefficients in xenon may reach very high values characteristic for collisional transitions between states coupled by a dipole-allowed transition. Estimates of the cross sections and rate coefficients based on the generalized Born approximation[15] for the most intense NIR $5p^5 6p_J \rightarrow 5p^5 5d_J, 7s_J$ transitions result in cross sections of the order of 10^{-15}–10^{-14} cm^2 at $T_e \geqslant 2$ eV.[16] At an electron temperature of $T_e \leqslant 5$ eV, and a plasma number density $N_e \leqslant 10^{11}$ cm^{-3}, which is typical for the medium power (0.5–5 kW) HET plume,[14,17] condition (9) becomes

$$A_i \gg 2 \times 10^4 \text{ s}^{-1}. \tag{10}$$

In the very near field of the plume and in the discharge region, the electron number density can exceed 10^{12} cm^{-3} and a large fraction of the electrons has energies $E_e \geqslant 7$–10 eV. At these conditions, significantly higher spontaneous emission rates are needed to satisfy the assumption of pure radiative decay,

$$A_i \gg 3 \times 10^6 \text{ s}^{-1}. \tag{11}$$

Even though the reported transition probabilities and excited state lifetimes in xenon differ significantly,[18–23] it can be concluded from examination of the upper levels of all prominent XeI and XeII emission lines in the HET plasma that they meet the condition (10) and, therefore, Eq. (7) applies to these lines in the HET plume. Since the strong XeII emission lines have very short radiative lifetimes, Eq. (7) can be applied to analyze the ionic emissions both in the HET plume and discharge. The list of XeI lines that could be described by Eq. (7) in the HET discharge and very near-field plume plasma is fairly limited. The prominent NIR lines associated with $5p^5 6p(p')$ upper levels, for which emission cross sections are reported in Part I of this article, are among the few XeI lines that meet condition (11).

The integrals in Eq. (7) represent the emission excitation rate coefficients. Equation (7) can be rewritten in terms of the excitation rates,

$$J_\lambda = \frac{hc}{4\pi\lambda} N_0 N_e \left(\sum_p \frac{N_p}{N_0} k_{ep}^\lambda + \frac{N_1}{N_e} k_1^\lambda + \frac{N_2}{N_e} k_2^\lambda \right), \tag{12}$$

where k_{ep}^λ is the emission excitation rate coefficient for electron collisions with particle in state p; k_1^λ and k_2^λ are the emission excitation rate coefficients for collisions of Xe^+ and Xe^{2+} with neutral xenon atoms, respectively, and N_p, N_1, and N_2 represent corresponding number densities. Given the low densities of higher charged ions in HET plasmas, only the singly and doubly charged xenon ions are taken into consideration.[24–26] Equation (12) neglects the excited ionic states and collisions of ions with metastable atoms. Presently, it is assumed that the respective rate coefficients are comparable with the respective ground state rate coefficients.

The excitation rate coefficients may be expressed directly through corresponding cross sections if the electron and ion energy distribution functions are specified. In the HET plasma, a Maxwellian distribution function is most commonly assumed for electrons. Ion energy distributions in the HET plume are featured by several peaks of different heights and widths.[24–26] Each peak represents a group of ions of different charge. The singly charged ions are the most abundant with a peak typically centered at an energy some tens of eV below $q \cdot e \cdot V$, where e is the electron charge and V is the thruster anode voltage. Doubly charged ion signals are noticeably weaker and located at about twice the energy of the singly charged ion peak. Widths of the peaks are about several tens of volts. In Part I we report that ion collision excitation cross sections, σ_1^λ and σ_2^λ, vary smoothly in the E/q range of 100–400 eV, with a slight incline with energy. Therefore, in a first approximation it can be assumed that the ionic cross sections are independent of energy within the range of the ion beam energy distribution in the HET plume. From these considerations, excitation rate coefficients can be determined from the electron temperature and the ion beam energy using

$$k_{ep}^\lambda = \int_0^\infty 2E_e \sqrt{\frac{2}{\pi (kT_e)^3 m_e}} \exp\left(-\frac{E_e}{kT_e} \right) \sigma_{ep}^\lambda (E_e) dE_e, \tag{13}$$

$$k_1^\lambda \approx \sigma_1^\lambda (\text{eV}) \sqrt{\frac{2eV}{M}}, \tag{14}$$

$$k_2^\lambda \approx \sigma_2^\lambda (2\ \text{eV}) \sqrt{\frac{4eV}{M}}, \tag{15}$$

where m_e is the rest mass of the electron and M is the atomic mass of xenon.

The number of parameters in equations (7) and (12) may be further reduced if plasma quasineutrality is taken into account, $N_e = N_1 + 2N_2$. Equation (7) then takes the form,

$$J_\lambda = \frac{hc}{4\pi\lambda} N_0 N_e \left(\sum_p \frac{N_p}{N_0} k_{ep}^\lambda + \alpha \cdot k_1^\lambda + \frac{1-\alpha}{2} k_2^\lambda \right), \tag{16}$$

where $\alpha = N_1/N_e$ is the ratio of the first ion (Xe^+) number density to the electron number density. Equation (16) can be defined more narrowly for specific species emissions. In the case of XeI emission lines, all XeII contributions can be eliminated from the equation, leading to

$$J_\lambda (\text{XeI}) = \frac{hc}{4\pi\lambda} N_0 N_e \left(k_{e0}^\lambda + \frac{N_m}{N_0} k_{em}^\lambda + \alpha \cdot k_1^\lambda + \frac{1-\alpha}{2} k_2^\lambda \right), \tag{17}$$

where k_{e0}^λ is the rate coefficient for process (1) involving ground state atoms; k_{em}^λ is the corresponding rate coefficient averaged for all metastable Xe atoms, and N_m is the Xe atom metastable number density.

The charge-state parameter, α, typically varies within a 0.7–0.95 range, depending on the thruster type and operating mode.[1,24,25] Relative abundances of the metastable atoms, N_m/N_0, and excitation rate coefficients, k_{em}^λ, have not been determined at HET plasma conditions. In order to circumvent this unknown parameter, the analysis can be limited to lines that are not coupled to metastable states through dipole-allowed transitions. For the NIR lines associated with the $2p_i$ [Paschen notation for $5p^5 6p(p')$ set of states] states, this would include the $2p_1$, $2p_3$, and $2p_5$ emission lines at 788.7, 834.7, and 828.0 nm, respectively. These lines are associated with radiative transitions to the XeI $5p^5 6s'(1/2)_1$ and $5p^5 6s(3/2)_1$ ($1s_2$ and $1s_4$ in the Paschen notation) states that are strongly optically coupled to the Xe ground state through a vacuum-ultraviolet transition. Rate coefficients for excitation of $2p_1$, $2p_3$, and $2p_5$ levels out of metastable states are considerably smaller than those for dipole-allowed transitions, and can be considered comparable with the rate coefficients k_{e0}^λ out of the ground state. This is confirmed by recent work by Jung *et al.* in studies of corresponding Kr levels.[27] As will become apparent from Eq. (26) below, if the metastable atom content in the HET plasma is below 1%, the second term in Eq. (17) may be ruled out when intensities of XeI 788.7, 834.7, and 828.0 nm are modeled. A XeI CRM based on these three-lines could thus be represented by

$$J_\lambda (\text{XeI}) = \frac{hc}{4\pi\lambda} N_0 N_e \left(k_{e0}^\lambda + \alpha \cdot k_1^\lambda + \frac{1-\alpha}{2} k_2^\lambda \right), \tag{18}$$

where all the terms can be computed from expressions (13)–(15) and the apparent emission cross sections reported in Part I. The disadvantage of this model is that it relies on relatively weak lines at 788.7 and 834.7 nm, making reliable intensity measurements more difficult. We, thus, consider it useful to derive a more general expression that takes metastable populations into account, thereby extending the number of lines available for analysis.

B. NIR CRM including emissions coupled to metastable levels

The strongest NIR lines are associated with $2p_i$ transitions to the $5p^5 6s(3/2)_2$ ($1s_5$) metastable state. Given the high oscillator strengths and low excitation energies out of this energy level to the radiating $5p^5 6p(2p_i)$ levels, rate coefficients, k_{em}^λ, may be orders of magnitude higher than k_{e0}^λ. This is fully confirmed by recent electron-impact studies of analogous levels in Kr.[27] Thus, excitation rates from states coupled to this metastable state through a dipole-allowed

transition can be comparable to excitation rates from the ground state, and must be considered if the more intense NIR lines are to be included in the CRM.

The steady-state equilibrium rate equation for a particular metastable state takes the form,

$$N_0\left(N_e k_{em} + \sum_q N_q k_{qm}\right) = N_m(\nu_{dm} + \nu_{cm}), \tag{19}$$

where k_{em} is the rate coefficient for excitation of the metastable level by electron impact, k_{qm} is the rate coefficient for excitation of the metastable level in a collision with the first ($q=1$) and second ($q=2$) ions, υ_{dm} is the frequency of metastable atom loss due to diffusion, and υ_{cm} is the frequency of the metastable atom loss due to collisions. Mityureva and Smirnov have shown that in case of excitation induced by electron-atom collisions metastable states such as the $1s_5$ state are predominantly populated through cascade transitions.[28] Since the collision-induced cascade rates are reflected by the apparent NIR emission cross sections reported in Part I, the source term in Eq. (19) can be approximated by

$$N_0\left(N_e k_{em} + \sum_q N_q k_{qm}\right) = N_0 N_e \sum_i \left(k^i_{e0} + \alpha \cdot k^i_1 + \frac{1-\alpha}{2} k^i_2\right), \tag{20}$$

whereby the sum on the right side of Eq. (20) occurs over all emission lines for which the lower state is the $1s_5$ ($J=2$) level. The selection rules for dipole transitions dictate that the upper states of the populating transitions are $1 \leqslant J \leqslant 3$ states. Thus, of the eight NIR lines, only those associated with upper states $2p_6(J=2)$, $2p_7(J=1)$, $2p_8(J=3)$, $2p_9(J=2)$, and $2p_{10}(J=1)$ need to be considered. We also neglect the emissions from np ($n>2$) states, because their intensities observed in HET and beam-induced spectra are much weaker in comparison with those from $2p_i$ states.

The wavelengths of the lines summed on the right side of Eq. (20) are $\lambda = 823.3$, 840.9, 881.9, 904.5, and 980.0 nm. Note that the 840.9 nm line involving the $2p_7$ level is associated with a very small branching ratio and, due to its weak intensity, is not recommended for diagnostic purposes. The respective 840.9 nm emission cross sections can be obtained from the 916.3 nm $2p_7$ line cross sections by applying the reported intensity ratio, I_{916}/I_{841} of 9.9.[29,30] The lower state of the 916.3 nm transition is the $1s_4$ state that is optically coupled to the ground state.

The accuracy of the total rate coefficient evaluation can be improved by representing the excitation rate coefficients in terms of relative units of one line in relation to all others coupled to the subject metastable state. For the evaluation of a XeI $2p$ emission line intensity of wavelength, λ, we introduce the function $K^\lambda(T_e, \alpha)$, which represents the ratio of the total excitation rate of the $1s_5$ state through emissions from the $2p$ states to the excitation rate through λ,

$$K^\lambda(T_e, \alpha) = \frac{\sum_i \{k^i_{e0} + \alpha \cdot k^i_1 + [(1-\alpha)/2]k^i_2\}}{k^\lambda_{e0} + \alpha \cdot k^\lambda_1 + [(1-\alpha)/2]k^\lambda_2}. \tag{21}$$

The sum in the numerator is the same as in Eq. (20). The relevant levels for the $1s_5$ coupled system are shown representatively in Fig. 1. Use of Eq. (21) then transforms Eq. (20) to

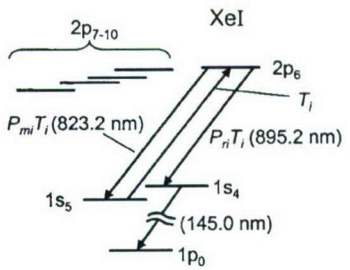

FIG. 1. Simplified level diagram of $2p_i$ state system based on the $2p_6$ example. $1p_0$: ground state; $1s_5$: metastable state; and $1s_4$: optically coupled to ground state. The figure identifies the transitions that play an important role in the stepwise excitation model.

$$N_0\left(N_e k_{em} + \sum_q N_q k_{qm}\right) = N_0 N_e \left(k^\lambda_{e0} + \alpha \cdot k^\lambda_1 + \frac{1-\alpha}{2} k^\lambda_2\right) K^\lambda(T_e, \alpha). \tag{22}$$

In the loss term in Eq. (19), it can be safely concluded that collisional depopulation of the metastable states is dominated by electron collisions. From the known Xe atom quenching rate coefficients[31] and due to the relatively small atom velocities, it can be concluded that the Xe atom quenching rate is much smaller than the electron collision quenching rate. At sufficiently high electron temperatures ($T_e > 1$ eV), electron-induced transitions to an upper $2p_i$ level are expected to be significantly more likely than superelastic collisions.[32] Because the rate coefficients for transitions between optically coupled levels are much higher than those for uncoupled levels, the collisional deexcitation rate υ_{cm} in Eq. (19) may be given by a sum of the excitation rate coefficients, T_i, corresponding to five $1s_5 \rightarrow 2p_i[J=1,1,2,2,3]$ transitions,

$$\nu_{cm} = N_e \sum_i P_{r_i} T_i, \tag{23}$$

where P_{r_i} are the branching coefficients for a radiative transition from the upper $2p_i$ state into the XeI $1s_4$ state that is optically coupled to the ground state (see Fig. 1). We assume that an atom excited to a $2p_i$ level has only two radiative transition pathways, either to the $1s_4$ state with probability P_{r_i} or to the $1s_5$ state with probability P_{m_i}. All other depopulation processes are neglected, so that $P_{r_i} + P_{m_i} = 1$ for all $2p_i$ levels.

Diffusion losses can be estimated from the thermal velocity, u_m, of the metastable atom and the scale length of the investigated plasma, L,

$$\nu_{dm} \approx u_m / L. \tag{24}$$

From the estimated excitation rate coefficients, k^λ_{em}, based on the Born approximation[15] and the recent work by Jung *et al.*,[27] and estimated diffusion loss frequencies, based on the direct simulation Monte Carlo/particle-in-cell (DSMC/PIC) calculations,[17] it can be concluded that the diffusion term can be neglected at typical HET conditions N_e

$>10^{11}$ cm^{-3}, $T_e>3$ eV in the discharge and $N_e>10^{10}$ cm^{-3}, $T_e>1.8$ eV in the plume,

$$\nu_{cm}=N_e\sum_i P_{r_i}T_i \gg \nu_{dm}. \tag{25}$$

Insertion of Eqs. (22) and (23) in Eq. (19) results in an expression for the relative metastable content, N_m/N_0,

$$\frac{N_m}{N_0}=\frac{\{k_{e0}^{\lambda}+\alpha\cdot k_1^{\lambda}+[(1-\alpha)/2]k_2^{\lambda}\}K^{\lambda}(T_e,\alpha)}{\sum_i P_{r_i}T_i}. \tag{26}$$

At these conditions, the metastable content is determined to be in the range of 0.01%–0.3%, depending on T_e, α and the thruster body scale.

Insertion of Eq. (26) in Eq. (17) provides the following expression for the emission intensity for a particular line of wavelength λ:

$$\begin{aligned}J_{\lambda}(\mathrm{XeI})&=\frac{hc}{4\pi\lambda}N_0N_e\left(k_{e0}^{\lambda}+\alpha\cdot k_1^{\lambda}+\frac{1-\alpha}{2}k_2^{\lambda}\right)\\&\quad\times\left[1+\frac{k_{em}^{\lambda}K^{\lambda}(T_e,\alpha)}{\sum_i P_{r_i}T_i}\right]\\&=\frac{hc}{4\pi\lambda}N_0N_e\left(k_{e0}^{\lambda}+\alpha\cdot k_1^{\lambda}+\frac{1-\alpha}{2}k_2^{\lambda}\right)\left[1+\frac{K^{\lambda}(T_e,\alpha)}{\zeta^{\lambda}}\right].\end{aligned} \tag{27}$$

The term $K^{\lambda}(T_e,\alpha)/\zeta^{\lambda}$ in Eq. (27) represents the fractional increase in intensity due to metastable population. The function, ζ^{λ},

$$\zeta^{\lambda}=\frac{\sum_i P_{r_i}T_i}{k_{em}^{\lambda}} \tag{28}$$

is the remaining unknown quantity that depends on an unknown excitation rate coefficient, k_{em}^{λ}. The metastable line excitation rate coefficient can be estimated from

$$k_{em}^{\lambda}=P_{\lambda}T_i, \tag{29}$$

where P_{λ} is the probability that the $2p_i$ state decays through radiation of wavelength λ. If the radiation is associated with a transition to the $1s_5$ metastable state, $P_{\lambda}\equiv P_{mi}$. Alternatively, for transitions from a $2p_i$ to the $1s_4$ state, $P_{\lambda}\equiv P_{ri}$. Because the $2p_i$ levels coupled to the $1s_5$ metastable state have similar energies, and the energy intervals between them and the $1s_5$ level are only approximately 1 eV, and because all excitation transitions are dipole allowed, we apply following approximation for the excitation rate coefficients, T_i,

$$T_i\propto 2J_i+1, \tag{30}$$

signifying that the transition rate coefficients are proportional to the degeneracy of the upper $2p_i$ level with total angular momentum quantum number, J_i. Based on this assumption, the ζ^{λ} function is given by

TABLE I. Parameters for $2p_i$ states optically coupled to the $1s_5$ metastable level (see Fig. 1). In case of the two transitions associated with the $2p_7$ level, the 840.9 and 916.3 nm lines are associated with the $1s_5$ and $1s_4$ lower states, respectively. P_{λ} is the branching ratio for radiative decay of the respective $2p_i$ level at wavelength, λ.

	$2p_6$	$2p_7$		$2p_8$	$2p_9$	$2p_{10}$
$2J_v+1$	5	3		7	5	3
P_{λ}	0.753	0.099	0.901	1.0	0.379	0.976
λ (nm)	823.2	840.9	916.3	881.9	904.5	980.0
ζ^{λ}	1.890	23.96	2.632	1.016	3.754	2.430

$$\zeta^{\lambda}=\frac{\sum_i P_{r_i}T_i}{P_{\lambda}T_j}=\frac{\sum_i P_{r_i}(2J_i+1)}{P_{\lambda}(2J_j+1)}. \tag{31}$$

The branching probabilities, P_{λ}, for the NIR lines associated with $2p_i$ levels that are coupled to the $1s_5$ level are shown in Table I. They were derived from the emission cross sections reported by Fons and Lin.[29] The resulting ζ^{λ} values are also listed.

C. Sample NIR model calculations

Equation (27) permits a simulation of the XeI NIR spectrum as a function of T_e and α. The cross sections reported for energies ranging from 10 to 70 eV in Part I are used. In order to extend the model to higher electron temperatures (>20 eV), we have taken the values reported by Fons and Lin for electron energies, E, between 70 and 150 eV at a nominal pressure $p=1$ mTorr and modeled them with the simple exponential (units in eV, mTorr),

$$\sigma_{\lambda}(E>70,p=1.0)=\sigma_{\lambda}(70,1.0)\left(\frac{E}{70}\right)^{c_{\lambda}}, \tag{32}$$

where the power c_{λ} is given in Table II. The zero-pressure cross sections are then obtained from the semiempirical expression derived in Part I,

$$\sigma_{\lambda}(E>70,0)=\frac{\sigma_{\lambda}(70,1.0)(E/70)^{c_{\lambda}}}{\{1+a_{\lambda}[(E-11.5/E-9.8)]^{n_{\lambda}}(1-e^{-\gamma_{\lambda}})^2\}}. \tag{33}$$

a_{λ}, n_{λ}, and γ_{λ} are line-specific parameters provided in Part I. This can be regarded as a crude estimate and a detailed analysis of the pressure dependence at the respective high electron energies is warranted to improve the model reliability at high values of T_e.

The $K^{\lambda}(T_e,\alpha)/\zeta^{\lambda}$ term is plotted in Fig. 2 as a function of T_e for the selected NIR lines that are associated with the upper states that are optically coupled to the $1s_5$ state. The fractional increases are calculated for a typical value of $\alpha=0.8$. Because the Xe^{2+} contribution to NIR emissions is

TABLE II. Exponential decay power, c_{λ}, for the selected NIR lines.

λ (nm)	788.7	823.2	828.0	834.7	881.9	904.5	916.3	980.0
c_{λ}	−0.607	−0.77	−0.589	−0.892	−1.07	−0.7	−0.473	−0.86

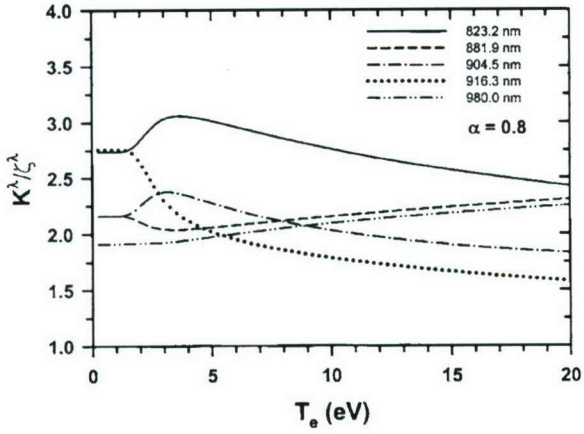

FIG. 2. The electron temperature dependence of the K^λ/ζ^λ factor for the five lines that are optically coupled with the $1s_5$ level.

much weaker than the Xe^+ contribution, and because α appears both in the numerator and the denominator in similar form, K^λ is only weakly dependent on α [see Eq. (21)]. From the graph it can be deduced that the fractional increase in emission intensity due to the inclusion of stepwise excitation via metastables ranges between ~150% and 300%.

The calculated relative line intensities are also weakly dependent on α, as is demonstrated in Fig. 3, where we compare for α=0.5 and 0.8 the emission rate ratios, $I_{\lambda 1}/I_{\lambda 2}$, between the 834.7 and 828.0 nm lines, which are uncoupled with the $1s_5$ metastable state (i.e., $K^\lambda=0$), and the 823.2 and 828.0 nm lines, where $K^{823}\neq 0$. There is a slight α dependence up to 5 eV, which is the temperature region where ion collisions produce significant emission rates. The ratios are strongly dependent on T_e over a significant temperature range, providing an accurate diagnostic between 1 and 10 eV. Below 1 eV, the ion contributions dominate, thus explaining the nearly temperature independent emission ratio between the 834.7 and 828.0 nm lines. The 823.2/828.0 line ratio plot is presented from 2 eV. At lower temperatures, Eq. (25) is no longer accurate and the 823.2 line cannot be modeled with Eq. (27). At very low temperatures below 1 eV, where ion collisions dominate over other excitation mechanisms, this ratio approaches the constant value of 7.6 and 7.9 for α=0.8 and α=0.5, respectively. These values are indicated by horizontal lines in Fig. 3 at low T_e. The high 823/828 ratio at low T_e derives from the significant Xe^+ emission cross sections at 300 eV for the 823.2 nm line radiance in comparison to the 828.0 nm line. Above 8 eV, the ion-impact contribution is negligible given the much larger fraction of electrons with energies above the excitation thresholds. At these energies, the ratios vary only slowly with T_e which can be attributed to the weaker energy dependence of electron emission cross sections at higher electron energies.

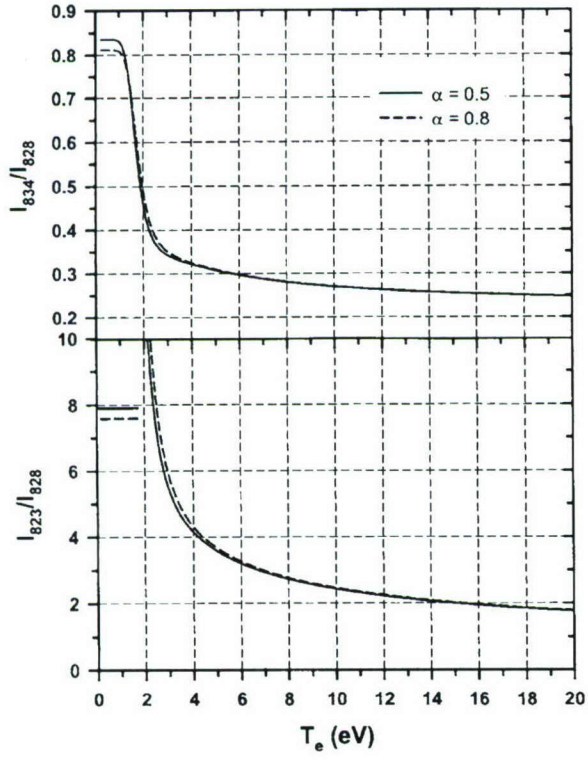

FIG. 3. Calculated electron temperature dependence of the intensity ratios of the XeI 834.7, 828.0, and 823.2 nm lines for α=0.8 and 0.5. The horizontal lines at low T_e in the bottom plot are the pure ionic emission ratios for the respective charge ratio parameters. The ratios of the bottom plot based on the present stepwise model are not applicable at low temperatures (<2 eV).

A computer program was written that uses a least-squares approach to adjust T_e, a pressure parameter signifying optical opacity (see Part I), and α to optimally reproduce a normalized set of the observed selected eight NIR line intensities. The performance of this model will be demonstrated on the D-55 anode layer thruster (TAL) data in Sec. IV.

D. Visible line diagnostics

The VIS plume spectra reported in Part I show prominent lines at 467.1 and 484.4 nm that are associated with the highest Xe^+ and Xe^{++} emission excitation cross sections. These lines can, therefore, be considered to diagnose α. Simple kinetic estimates, however, lead to the conclusion that XeII line excitation in the VIS spectrum must have very important contributions from process (3), even at relatively low electron temperatures. Thus, a proper analysis would require knowledge of the respective electron-ion emission excitation cross sections. Furthermore, the 484.4 nm line lies very close to a $6s-7p$ XeI line at 484.3 nm. Consequently, a high-resolution experiment is necessary for an accurate analysis.

Despite the fact that cross sections for electron-ion excitation processes are not accurately known, we can state that the emission excitation rates that depend on the electron temperature should remain constant in regions of electron gas isothermicity. Therefore, XeII line emission intensities should be proportional to the number densities of the colliding species;

$$J_\lambda \sim N_e N_1 \sim \alpha N_e^2. \quad (34)$$

Hence, disregarding the variation of α in the regions, where the electron temperature is almost constant, the charged particle number density distribution may be derived from the XeII emission intensity measurement as, $N_e \sim N_1 \sim \sqrt{J_\lambda}$.

III. EXPERIMENT

Optical spectra of the TAL were recorded at the TSNII-MASH test facility. The test facility has a 1.8 m diameter and is 4 m long. It was pumped by five oil diffusion pumps, which resulted in a base pressure of $1-2\times10^{-6}$ Torr. During the operation of the TAL, the base pressure grew to 2×10^{-5} Torr (Xe reference). A more detailed description of the facility has been reported previously.[33] The vacuum chamber was equipped with a big window for optimal data acquisition in the TAL near-field plume and discharge regions. General features of the TALs as well as detailed information about their design and performance characteristics may be found in the literature.[11–14]

The spectra discussed in this particular work were recorded with two instruments. The first was the asymmetric Ebert-Fastie 0.5 m F/6 scanning monochromator equipped with a commercial photomultiplier tube that was described in Part I. This instrument was primarily used for qualitative analysis of the TAL spectra and comparison of the spectra with the beam experiment. The entrance and exit slits of the monochromator were set between 0.05 and 0.4 mm to optimally meet the requirements of high signal-to-noise ratio and satisfactory spectral resolution. Thus, the slit width was widened for the weaker plume region compared with the high intensity discharge region. The spectral resolution of the monochromator varied from about 0.1 nm in the discharge to 1 nm in the plume region.

The quantitative studies presented here were carried out with a charge-coupled device (CCD)-based spectrometer. A S2000 Ocean Optics spectrometer with 600 groove/mm grating was used. The use of a 25 mm slit results in a spectral resolution of about 1.2 nm. The wide dynamic range of the CCD ($\sim10^5$) allowed utilization of the spectrometer both for discharge and plume measurements. The entire radiation spectra were measured instantaneously along spans (chords) of a selected cross section perpendicular to the TAL plume axis. The spectrograph of the analyzer acquired radiation through a fiber optic cable equipped with a lens at its sensing end. The lens could be translated in the vertical direction by a precise stepper motor mechanism while observing the radiation along horizontal lines of sight, as illustrated in Fig. 4. The optical system ensured about a 2 mm spatial resolution in the discharge and near-field regions and 5–7 mm in the plume regions, respectively. The plume region was located 100–200 mm downstream from the thruster exit plane. Integral (span ward) radiation of selected spectral lines of interest along different lines of sight could be easily extracted from these measurements. Radial dependences of the specific radiation for selected lines were reconstructed from the span-ward profiles with the use of the standard Abel deconvolution procedure.[4] The wavelength and spectral sensitivity of the optical multichannel analyzer were determined in the same way as described for the monochromator instrument in Part I.

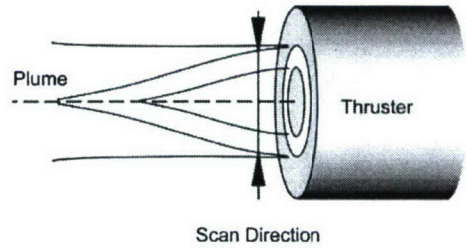

FIG. 4. Experimental measurement geometry. The scan direction indicates the motion of the fiber optical sensor cable when radial profiles are measured.

IV. RESULTS

A. Electron temperature measurements

As mentioned in Sec. II, the most appropriate diagnostics would use emission lines uncoupled from metastable states to avoid errors introduced by approximations of the metastable state excitation functions. In the case of the NIR lines, however, the uncoupled emission lines at 788.7 and 834.7 nm exhibit relatively low excitation cross sections, making measurements problematic in the plume region where plasma radiation is weak. In order to test the model for consistency, we compare electron temperatures derived using Eq. (18) from the observed ratio, I_{834}/I_{828}, and using Eq. (27) from the observed ratio, I_{823}/I_{828}. Both intensity ratios I_{834}/I_{828} and I_{823}/I_{828} were measured in the TAL D-55 discharge and along the plume axis. The thruster was operated at an anode voltage of 300 V, and a discharge current of 3.2 A. The electron temperature was derived from the modeled intensity ratios shown in Fig. 3 for $\alpha=0.8$ and assuming optically thin conditions. Results of these measurements are tabulated in Table III and plotted in Fig. 5. Electron temperature measurements from a Langmuir probe[32] are also shown at larger axial distances. The window position in the TAL test chamber precluded measurements at axial distances exceeding 200 mm, thus preventing a direct comparison of the probe measurements, which were taken at 300 mm and higher.

All of the temperatures derived from the I_{834}/I_{828} ratio are lower than the corresponding values from the I_{823}/I_{828} ratio. The sources of the discrepancy will be discussed in Sec. V. At 5 mm, where the discharge of the TAL is probed at a radial distance corresponding to the annulus, a high electron temperature exceeding 50 eV is derived, while at larger axial distances, the electron temperature drops to values between 2.9 and 5 eV along the axis of the thruster. Except in the discharge, where the electron temperature is high, and, therefore the two-line approach is less accurate, the agreement between the two derivations is good, validating the present treatment of effects due to metastable stepwise excitation mechanisms. In the far field, the agreement with the Langmuir probe measurements is also very satisfactory.

The pressure dependence of the two-line approach is tested by comparing the derived temperatures assuming a

TABLE III. Measurements of intensity ratios and derived electron temperature for a D-55 TAL, operated at an anode voltage of 300 V, and a current of I=3.2 A. The 25 mm radial position corresponds to the thruster annulus.

Position		TAL			T_e (eV)/CRM	
Axial (mm)	Radial (mm)	I_{834}/I_{828}	I_{823}/I_{828}	I_{834}/I_{828}	I_{823}/I_{828}	eight line
5	25	0.231	1.125	50	>70	>70
25	25	0.311	3.35	4.86	5.74	6.1±0.9
25	0	0.332	3.89	3.63	4.58	4.9±0.7
50	0	0.346	4.48	3.13	3.83	4.29±0.53
100	0	0.354	4.64	2.94	3.68	3.86±0.42
200	0	0.355	4.74	2.92	3.61	3.39±0.32

nominal pressure of 1.5 mTorr corresponding to the optical conditions of the beam experiment in Part I. Not surprisingly, there is almost no effect in the plume where the electron temperatures are insufficient to cause excitation at energies where cascading and the resulting radiation trapping effects are significant. Furthermore, ion collisions are very important at low temperatures, and they do not exhibit radiation-trapping effects (see Part I). In the discharge at 5 mm, however, the derived electron temperature from the 834/828 ratio is lowered to 13 eV, while that for the 823/828 ratio descends to 50 eV at 1.5 mTorr. Since the dense discharge region is most likely to exhibit signs of optical opacity, radiation trapping effects must be considered an additional source of error for the discharge.

Given the errors in intensity measurement and in the measured emission cross sections of Part I, and the approximations associated with the present pressure dependence (Part I) and metastable contribution model, the accuracy of T_e is expected to increase with the number of lines included in the analysis. Figure 6 shows the results of an eight-line analysis assuming optically thin conditions on selected NIR lines associated with different $2p_v$ levels. The measurements are taken at axial distances of 5 and 200 mm (discharge and plume, respectively). The measured lines, I_i^{TAL}, and those corresponding to the best-fit electron temperature, I_i^{RM}, are normalized to 1. In both cases, an ion charge parameter, α =0.8, and optically thin conditions are assumed.

The calculation of a matrix, (T_e, α, χ^2), where χ^2 is the relative average least squares given by

$$\chi^2 = \frac{1}{n}\sum_{i=1}^{n} \frac{(I_i^{\mathrm{TAL}} - I_i^{\mathrm{SRM}})^2}{(I_i^{\mathrm{TAL}})^2}, \tag{35}$$

and n is the number of lines in the analysis, shows that T_e is only weakly dependent on α. A temperature of 3.39±0.32 eV minimizes χ^2 in the plume (200 mm axial distance). The errors are the statistical 90% confidence limits assuming a standard deviation of 10% for all of the measured line intensities, a highly conservative intensity accuracy. Variation of α results only in minor differences (<6%) when varied from 0.5 to 1.0 for the plume measurement. In

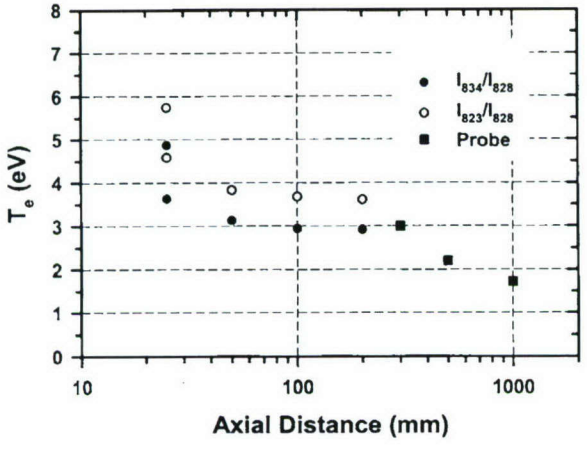

FIG. 5. Electron temperatures along the D-55 thruster axis reduced from measurements of the respective XeI line intensity ratios, at an operating condition of V=300 V, I=3.2 A. The optical diagnostic data, assuming α=0.8, are compared with the Langmuir probe measurements at large axial distances.

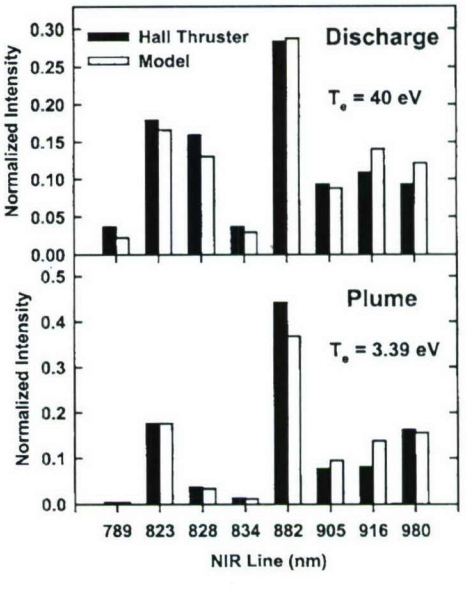

FIG. 6. Comparison between observed and modeled NIR line intensities for discharge (5 mm axial distance) and plume (200 mm axial distance) radiances. The intensities of the measured and modeled spectra are normalized to 1. The associated electron temperatures, determined assuming α=0.8, are the result of a least-squares fit for the plume and are fixed at 40 eV, for the discharge, where no least-squares minimum is found below 70 eV.

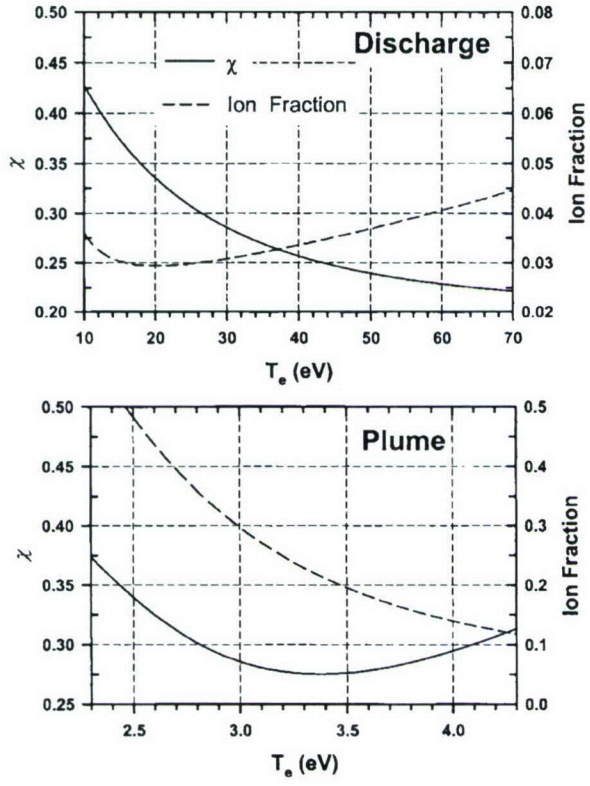

FIG. 7. Standard deviation and ion fractional radiance contribution as a function of electron temperature determined from the eight-line NIR model calculations of the plume and discharge line intensities.

the discharge (5 mm distance from thruster plane outside annulus), however, no χ^2 minimum is found between 1 and 70 eV. We compare the discharge measurement in Fig. 6 with a set of spectral intensities calculated for T_e=40 eV. At this energy, 99.8% of the Maxwellian electron energy distribution is below 300 eV, the maximum energy for which we have incorporated cross sections in the model.

The sensitivity of the eight-line approach is demonstrated in Fig. 7, where the relative standard deviation, χ, is plotted versus T_e for the two measurements. The figure also plots the fraction of the total radiance attributable to ion collisions. While there is not a χ minimum in the applicable electron temperature range for the discharge, it is well defined for the plume. At the derived plume T_e of 3.39 eV, 22% of the radiance from the selected eight-line analysis can be attributed to ion collisions. While the ion contribution drops as expected with T_e near the plume temperature, at higher electron temperatures the calculated ion contribution is seen in the top panel to increase again after reaching a minimum of 3% at 20 eV. This can be attributed to the decreasing emission cross sections with energy as T_e increases, and the decreasing fraction of electrons in an energy range where the emission excitation cross sections are very high.

TABLE IV. T_e (eV) determinations in the TAL plume (200 mm axial distance) and discharge (5 mm axial distance) using the present CRM model. "eight lines" corresponds to a fit to the experimental eight NIR lines listed in Table II using the full CRM model including ion and metastable contributions. "Three lines" refers to the full CRM model that only includes the emission transitions that are not coupled to the metastable $1s_5$ state. "No ions" is a model that does not include ion collision contributions. "No meta" identifies the results if effects due to metastables are neglected (K^{λ}=0). The errors are the statistical 90% confidence limits assuming a 10% standard deviation in the TAL data points.

	T_e (eight lines)	T_e (three lines)	T_e (no ions)	T_e (no meta)
Plume	3.39±0.32	2.74±0.06	2.49±0.40	1.61±0.21
Discharge	>70	40±30	>70	10.5±2.2

The results of the TAL evaluations are summarized in Table IV where calculations for an eight-line analysis are compared with a three-line analysis involving only the $2p_1$, $2p_3$, and $2p_5$ emission lines that are not coupled to the $1s_5$ metastable state, and eight-line models that neglect ion contributions (no ions) and metastables (no meta). In the case of the plume measurement, the three-line model produces a slightly lower value of T_e than the eight-line analysis. Variation of the effective pressure between 0.1 and 1.5 mTorr leads to negligible changes in the derived electron temperature. Again this can be attributed to the fact that at low electron temperatures, the electron-impact and ion-impact radiation processes are not strongly affected by radiation trapping. The determined temperatures from eight-line analyses that neglect ion collisions and metastables are significantly lower for the plume models. The effect of neglecting metastables is particularly large. Neglecting both metastables and ions leads to a further reduction in the derived electron temperature in the eight-line analysis.

Similarly, neglecting metastable contributions when modeling the discharge spectrum results in the determination of a much lower discharge temperature of ~10 eV. Neglecting ions does not affect the analysis due to the small ion contribution at high T_e. As in the plume case, a three-line analysis produces a lower value of T_e, however, the accuracy of the determination, demonstrated by the large error of ±30 eV, is very low. Assuming a higher effective pressure of 1.5 mTorr results in a lower temperature of 51±24 eV, which is similar to the observation made in the two-line analysis above.

B. Plasma density measurements

Figure 8 shows a radial profile of the I_{823}/I_{828} ratio, measured at a distance of 5 mm from the D-55 thruster exit plane. Interestingly, the ratio is almost constant across the discharge where one may assume that the electron temperature stays constant. Isothermicity of the electron gas in the near discharge region that is limited by a 20–40 mm radial distance (the annulus position is schematically shown by dashed vertical lines) was also demonstrated by measurements of the electron temperature profile covering a 10 mm section by Domonkos *et al.*[14] At this condition Eq. (34) may be applied. Figure 9 shows a charged-particle radial density profile determined from this equation at 5 mm from the D-55 TAL (the dashed vertical lines again point out the annulus position). The Xe ionic line XeII 541.9 nm was used for these measurements. Utilization of other XeII lines from the VIS spectral region results in very similar profiles. The maximum of the charge density on the radial profile is slightly

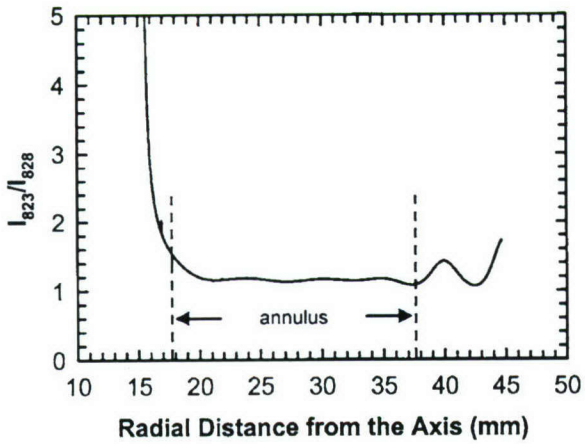

FIG. 8. Line intensity ratio measurements, I_{823}/I_{828}, across the D-55 TAL discharge (5 mm from the thruster exit). The thruster was operated at $V=300$ V, $I=3.2$ A. The radial position of the annulus is indicated with vertical dashed lines.

shifted from the annulus center towards the thruster axis. A similar observation has been reported by Haas and Gallimore in an SPT using a fast Langmuir probe.[34]

V. DISCUSSION

The emission excitation cross sections reported in Part I have been incorporated into a collisional radiative model covering the prominent NIR XeI lines. These lines are associated with emission rates that exceed 3×10^6 s^{-1} and, therefore, the model can neglect depopulation processes other than radiative decay. This CRM for the Hall thruster plasma radiation diagnostics includes both ion collisional excitation mechanisms as well as an approach to account for the effect of stepwise excitation mechanisms involving metastables. The model is applied to sample spectra observed from the discharge and plume of a D-55 TAL thruster operating in a ground-based test facility.

A least squares fit of the electron temperature at fixed ion charge ratios and pressures leads to satisfactory reproduction of the selected NIR line intensities observed at various locations outside of the thruster exit plane. The derivation at low electron temperatures appears only weakly dependent on the

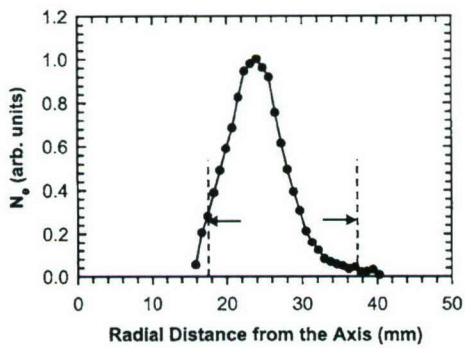

FIG. 9. Radial distribution of the charge density at an axial distance of 5 mm as measured from the 541.9 nm XeII line. The D-55 TAL was operated at $V=300$ V, $I=3.15$ A. The radial position of the annulus is indicated with vertical dashed lines.

unknown charge ratio, α, and radiation trapping effects are not significant provided zero-pressure extrapolated cross sections, as reported in Part I, are used. The model extracts electron temperatures that are consistent with values typically quoted for such engines, in particular, for the near-field plume region.[11,14,35] The electron temperatures also agree with Langmuir probe measurements determined for the same thruster at the same operating conditions. Similar values of $T_e\approx2.6$ eV were previously measured at an axial position of 300 mm from the exit plane of the D-55 thruster using a Langmuir probe by Karabadzhak *et al.*[35] Domonkos *et al.*[14] measured radial profiles of electron temperature at several axial distances from a D-55 thruster. At 20 mm, they report an axial electron temperature of 3.5 eV, while at a radial distance corresponding to the annulus, the temperature climbs to 5.7 eV. These measurements are comparable with present values of 4.9 ± 0.7 and 6.0 ± 0.9 eV, respectively, determined in the eight-line analysis at 25 mm (Table III). Similar temperatures have been modeled by Karabadzhak *et al.*[35] and were also used as input for successful computations of the D-55 thruster plume parameters by DSMC-PIC methods.[17]

Closer to the thruster, probe measurements[11,14] result in electron temperatures exceeding 10 eV. Garner *et al.* [11] reports that the temperature increases up to 80 eV and higher in the discharge, again consistent with the present model and observations. High TAL discharge temperatures have also been predicted by Choueiri.[36] Domonkos *et al.*[14] reported a non-Maxwellian behavior of the probe current in this near-field region. At such conditions it can be expected that probe and optical measurements produce different results since probes tend to be more sensitive to the energy distribution of low-energy electrons, while the optical measurements provide a measure of the electron energy distribution above threshold. From inspection of the two-line intensity ratios shown in Fig. 3, it can be concluded that the intensity ratios predicted by the NIR model become insensitive to electron temperature variations beyond 15–20 eV. A more accurate model of higher electron temperatures would depend on an analysis of visible emission lines, including XeII lines. A model including the latter depends on emission cross sections for electron impact excitation of Xe^+, which are not available.

As seen in Fig. 2, inclusion of metastables results in ~300% increase in the modeled emission intensity of the 823.2 nm line. Comparison of the present model with calculations that either neglect ion contributions or stepwise metastable excitation exhibit marked differences in the derived electron temperature, generally leading to significantly lower values (see Table IV), if not complete failure to reproduce the spectrum. This work, in conjunction with our earlier report,[9] establishes the importance of ion-atom collisions in a Hall thruster radiative model. The present model suggests that ~30% of the NIR radiance is due to ions at a typical plume temperature of 3 eV. The ion-collision contributions are a direct consequence of the large $Xe^+ + Xe$ NIR emission excitation cross sections reported in Part I, and the significant differences observed in the ion and electron-induced spectral intensity distributions due to the different excitation

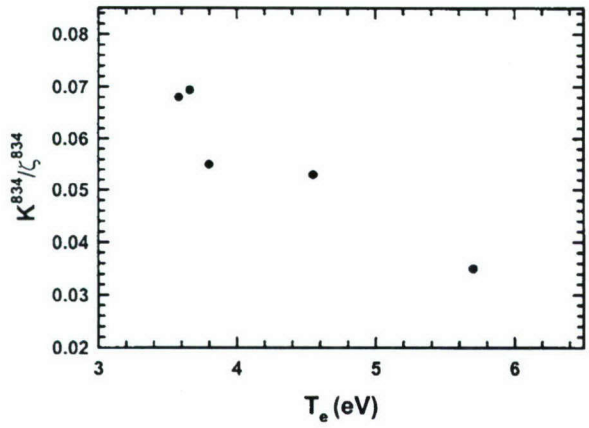

FIG. 10. Correction factor, $K^{\lambda}/\zeta^{\lambda}$, for uncoupled line, $\lambda=834.7$ nm, that brings T_e determined from the I_{834}/I_{828} ratio in agreement with that determined from I_{823}/I_{828}.

mechanisms. Consequently, intensity ratios between particular line pairs change dramatically as T_e is increased from low values, where ion impact dominates the spectrum, to values where electron impact is the primary source of NIR radiance.

The discrepancy between the electron temperatures derived using the I_{823}/I_{828} and I_{834}/I_{828} intensity ratios is symptomatic of the fact that the current model is still incomplete. Likely sources of the discrepancy are the assumption of Eq. (30), which provides an estimate for the relative line excitation cross sections from the $1s_5$ metastable state, and the approximation that those lines that are not coupled to the $1s_5$ level do not experience an enhancement due to some stepwise excitation mechanism. While there have been no measurements or calculations of emission excitation cross sections out of metastable states of Xe, there are reasons to reevaluate the latter assumption for the $2p_1$ (788.7 nm) and $2p_3$ (834.7 nm) lines that the model considers uncoupled from metastable states. These levels are associated with the $J=1/2$ ion core limit, i.e., they are referred to as $6p'$ states, and are mixed with $3p_i$ levels associated with the $J=3/2$ ion core limit, or $3p_i(7p)$ states, as evidenced by emissions from $6p'$ to $6s$ and from $7p$ to $6s'$ levels. Consequently, while the $2p_1$ and $2p_3$ $6p'$ levels are decoupled from the $1s_3(6s')$ metastable state, they are not fully decoupled from the $1s_5(6s)$ metastable state. Thus, the associated 788.7 and 834.7 nm lines are expected to be enhanced through a stepwise mechanism, while the $2p_5(6p)$ 828.0 nm line is not.

In order to assess the magnitude of the enhancement, the $K^{\lambda}/\zeta^{\lambda}$ term [Eq. (27)] of the $\lambda=834.7$ nm line is raised from zero to bring the derived value of T_e based on the I_{834}/I_{828} ratio in agreement with that based on I_{823}/I_{828}. The thus derived K^{834}/ζ^{834} values for the I_{834}/I_{828} measurements of Table III are plotted in Fig. 10. Interestingly, a decline is observed from a value of $\sim 7\%$ at ~ 3.6 eV to a value of 3.5% at 5.7 eV. This is consistent with the forbidden nature of the $1s_5(6s)-2p_3(6p')$ transition, where the electron energy dependence of the excitation cross section can be expected to exhibit a sharp maximum above threshold with a rapid decrease at higher energies where spin-changing collisions become less probable.

The discharge data point in Fig. 7, representing an electron temperature larger than 70 eV as obtained from the I_{823}/I_{828} analysis, is not shown. A mere 2% enhancement of the I_{834}/I_{828} ratio in the discharge would result in an increase of the derived T_e from 50 to 70 eV. This clearly suggests that this ratio is not suitable for an analysis at high electron temperatures. The minor enhancements required to bring the temperatures derived from the I_{834}/I_{828} and I_{823}/I_{828} ratio analyses into agreement are consistent with the weaker coupling and the higher respective $1s_5 \rightarrow 2p_3(6p')$ excitation energies, leading to lower cross sections. Incorporation of a 7% 834.7 nm line enhancement in the eight-line analysis of the 200 mm plume measurement results in only a negligible reduction in the derived temperature of 3.36 ± 0.32 eV compared with the uncorrected value of 3.39 ± 0.32 eV.

The enhancement of the 788.7 nm line can be expected to be even less due to the lower degeneracy ($J=0$) of this state. Arbitrarily setting the enhancement to half that of the 834.7 nm line results again in a negligible reduction of the derived temperature. From the above it can be concluded that the $2p_i(6p')$ lines are indeed slightly affected by a stepwise mechanism, but the correction does not affect significantly the eight-line analysis. Overall, given the weakness of the 788.7 and 834.7 nm lines, the error in the intensity measurement can be regarded comparable to the enhancement due to stepwise excitation. The present TAL measurements have detected interference from an additional line near 834.7 nm, most likely the $6p^2D^0_{5/2} \rightarrow 5d^2F^0_{7/2}$ emission line of Xe II. This interference was not resolved in the experiments that measured the cross sections. Although the interference was taken into account in the TAL measurements, it adds to the error of the derived intensity of this weak line. This further emphasizes the need for an analysis based on several, intense, $2p_i$ lines such as the present eight-line analysis, thereby mitigating errors in intensity derivations as well as errors in the cross sections and associated pressure dependences reported in Part I.

The most important shortcoming of the present CRM is the inability of modeling XeII emission intensities in the VIS and UV spectra. This is attributed to the complete absence of accurate calculations or measurements of e^-+Xe^+ emission excitation cross sections. A set of electron-impact XeII emission cross sections, similar to those reported in Part I, would provide a wider choice of transitions that should also improve the accuracy at high electron temperatures due to the higher excitation thresholds of the respective ionic levels.

Nevertheless, the charge density distribution can be derived in the TAL discharge based on the electron gas isothermicity assumptions of Eq. (34). The peak of the distribution is slightly shifted from the annulus center toward the thruster axis. Such behavior of the charge density distribution is often observed in TALs. It demonstrates a tendency to form a high-density plasma region along the axis in the very near plume field. This region is conventionally called "crossover" and is readily observed by the naked eye. Outside the isothermicity region the results may only have a qualitative character. As Fig. 8 illustrates, the intensity ratio and electron temperature is highly variable closer to the axis. At large axial distances the approach based on the assumption that process (3) is the only contributor is expected to fail, as well. Even if the con-

dition of electron gas isothermicity holds at large distances, the charge-ratio parameter, α, may vary in the radial direction due to the dependence of the angular ion intensity distributions on charge state.

The ion-Xe impact may also produce a significant fraction of XeII radiance at low electron temperatures. A reduction of ion-impact interference can be achieved by basing the analysis on XeII lines that have low ion-impact cross sections such as the 504.5 nm line (see Part I). That line, however, is barely detected in the plume spectrum. In the VIS region, the latter spectrum does in fact closely resemble the Xe^{2+}-impact spectrum, suggesting further that process (3) is not the sole contributor to XeII lines in the far field. As mentioned in Part I, a detailed analysis of these conditions could lead to a CRM for the visible emissions that would result in the additional diagnostic of ion charge ratios in the plume. This work is reserved for future research.

VI. CONCLUSION

This paper represents an attempt at incorporating a broad set of emission excitation cross sections in a CRM for HET Xe plasmas. A detailed model is presented for a set of intense NIR emission lines. The model establishes the importance of ion processes in producing emissions at plasma electron temperatures below 5 eV. The model also takes a stepwise excitation via metastables into account. Due to the markedly different NIR spectra produced by ions and electrons, the method is particularly accurate at low temperatures where ionic contributions are important, and thus line ratios depend strongly on the effective electron temperature. The diagnostic presents a choice of measuring eight selected NIR lines associated with the $2p_i$ (Paschen notation) upper levels, or just two lines for which the intensity ratio is highly T_e dependent. An eight-line analysis is recommended in order to overcome inaccuracies in the pressure dependent effective cross sections and plasma line intensity measurements. For a simple two-line analysis, the 823.2 and 828.0 nm lines are recommended due to their close spectral proximity, thereby minimizing the spectral sensitivity calibration errors, and due to the significant T_e dependence at low temperatures. The present application of the model to TAL D-55 measurements yields T_e values that are within errors in agreement for the recommended two-line and eight-line approaches. It is also demonstrated that spatial plasma density distributions can be determined from XeII line intensities at regions of high electron temperatures.

ACKNOWLEDGMENTS

The work has been supported by AFOSR through task 2303EP02 (Program Manager: Dr. Michael Berman) and by EOARD through ISTC Partner Project No. 2370 (Program Manager Dr. Ingrid Wysong).

[1]D. J. Manzella, *23rd International Electric Propulsion Conference, Columbus, OH, 1993*, Report No. IEPC-93-097, 2003.
[2]G. F. Karabadzhak, A. V. Semenkin, A. O. Tverdokhlebov, and D. J. Manzella, Proceedings of 25th International Electric Propulsion Conference, Cleveland, OH, 1997 (unpublished).
[3]A. I. Bugrova, V. A. Ermolenko, and A. S. Sokolov, Teplofiz. Vys. Temp. **25**, 1080 (1987).
[4]H. G. Griem, *Plasma Spectroscopy* (McGraw-Hill, New York, 1964).
[5]P. Leray, J. Bonnet, D. Pigache, T. Minea, J. Bretagne, and M. Touzeau, *25th International Electric Propulsion Conference, Cleveland, OH, 1997*, Report No. IEPC 97-054, 1997.
[6]G. Colonna, L. D. Pietanza, and M. Capitelli, *31st AIAA Plasmadynamics and Lasers Conference, Denver, CO, 2000*, AIAA Report No. AIAA-2000-2349, 2000.
[7]N. B. Meezan, J. W. A. Hargus, D. P. Schmidt, and M. A. Cappelli, *35th AIAA/ASME/SAE/ASEE Joint Propulsion Conference, Los Angeles, CA, 1999*, AIAA Report No. AIAA-99-2284, 1999.
[8]M. Prioul, S. Roche, D. Pagnon, L. Magne, M. Touzeau, A. Bouchoule, and P. Lasgorceix, *37th AIAA/ASME/SAE/ASEE Joint Propulsion Conference and Exhibit, Salt Lake City, UT, 2001*, AIAA Report No. AIAA-2001-3358, 2001.
[9]G. F. Karabadzhak, Y. Chiu, S. Williams, and R. A. Dressler, *37th AIAA/ASME/SAE/ASEE Joint Propulsion Conference and Exhibit, Salt Lake City, UT, 2001*, AIAA Report No. AIAA-2001-3893, 2001.
[10]Y. Chiu, B. L. Austin, S. Williams, R. A. Dressler, and G. F. Karabadzhak, J. Appl. Phys. **99**, 113304 (2006).
[11]C. E. Garner, J. R. Brophy, and J. E. Pollack, *30th AIAA/ASME/SAE/ASEE Joint Propulsion Conference, Indianapolis, IN, 1994*, AIAA Report No. AIAA-94-3010, 1994.
[12]C. E. Garner, S. O. Tverdokhlebov, A. V. Semenkin, and V. I. Garkusha, *32nd AIAA/ASME/SAE/ASEE Joint Propulsion Conference, Lake Buena Vista, FL, 1996*, AIAA Report No. AIAA-96-2967, 1996.
[13]D. J. Manzella, S. Oleson, J. Sankovic, T. Haag, A. Semenkin, and V. Kim, *32nd AIAA/ASME/SAE/ASEE Joint Propulsion Conference, Lake Buena Vista, FL, 1996*, AIAA Report No. AIAA-96-2736, 1996.
[14]M. T. Domonkos, A. D. Gallimore, C. M. Marrese, and J. M. Haas, J. Propul. Power **16**, 91 (2000).
[15]I. I. Sobelman, L. A. Vainshtein, and E. A. Yukov, *Excitation of Atoms and Broadening of Spectral Lines*, 2nd ed. (Springer, New York, 1998).
[16]L. A. Vainstein and I. L. Beigman (unpublished).
[17]I. D. Boyd, J. Propul. Power **16**, 902 (2000).
[18]J. Sabbagh and N. Sadeghi, J. Quant. Spectrosc. Radiat. Transf. **17**, 297 (1977).
[19]L. Allan, D. G. Jones, and C. Schofield, J. Opt. Soc. Am. **59**, 842 (1969).
[20]M. H. Miller, R. A. Roig, and R. D. Bengtson, Phys. Rev. A **8**, 480 (1973).
[21]W. L. Wiese and G. A. Martin, Natl. Bur. Stand. Ref. Data. Sec., Natl. Bur. Stand. (U.S.) Circ. No. 68 (U.S.GPO, Washington, D.C., 1980), Vol. 11.
[22]I. Martin, C. Hernando, C. Lavin, and A. M. Velasco, J. Quant. Spectrosc. Radiat. Transf. **62**, 71 (1999).
[23]V. R. Lazovskaya and G. K. Tumakaev, Zh. Tekh. Fiz. **49**, 573 (1979).
[24]F. S. Gulczinski and A. D. Gallimore, J. Propul. Power **17**, 418 (2001).
[25]L. B. King and A. D. Gallimore, J. Propul. Power **16**, 1086 (2000).
[26]J. E. Pollard and E. J. Beiting, Third International Conference on Spacecraft Propulsion, Cannes, France, 2000 (unpublished).
[27]R. O. Jung, T. E. Stone, J. B. Boffard, L. W. Anderson, and C. C. Lin, Phys. Rev. Lett. **94**, 163202 (2005).
[28]A. A. Mityureva and V. V. Smirnov, J. Phys. B **27**, 1869 (1994).
[29]J. T. Fons and C. C. Lin, Phys. Rev. A **58**, 4603 (1998).
[30]A. A. Radzig and B. M. Smirnov, *Reference Data on Atoms, Molecules, and Ions* (Springer-Verlag, Berlin, 1985).
[31]N. Sadeghi and J. Sabbagh, Phys. Rev. A **16**, 2336 (1977).
[32]A. G. Zhiglinski, *Handbook for Elementary Processes Involving Atoms, Ions, Electrons and Protons* (St. Petersburg University, St. Petersberg, 1994).
[33]L. E. Zakharenkov, A. V. Semenkin, and A. V. Kochergin, 28th International Electric Propulsion Conference, Toulouse, France, 2003 (unpublished).
[34]J. M. Haas and A. D. Gallimore, Phys. Plasmas **8**, 652 (2001).
[35]G. F. Karabadzhak, A. V. Semenkin, and A. O. Tverdokhlebov, Third European International Propulsion Conference, Cannes, France, 2000 (unpublished).
[36]E. Y. Choueiri, Phys. Plasmas **8**, 5025 (2001).